Journal of Materials Chemistry

Cite this: J. Mater. Chem., 2011, 21, 9332

www.rsc.org/materials

PAPER

Single-crystalline MoO_3 nanoplates: topochemical synthesis and enhanced ethanol-sensing performance†

Deliang Chen,*[ab] Minna Liu,[a] Li Yin,[a] Tao Li,[a] Zhen Yang,‡[a] Xinjian Li,[b] Bingbing Fan,[a] Hailong Wang,[a] Rui Zhang,[ac] Zhengxin Li,[ad] Hongliang Xu,[a] Hongxia Lu,[a] Daoyuan Yang,[a] Jing Sun[e] and Lian Gao[e]

Received 6th April 2011, Accepted 12th April 2011
DOI: 10.1039/c1jm11447f

Molybdate-based inorganic–organic hybrid disks with a highly ordered layered structure were synthesized *via* an acid–base reaction of white molybdic acid ($MoO_3 \cdot H_2O$) with *n*-octylamine ($C_8H_{17}NH_2$) in ethanol at room temperature. The thermal treatment of the as-obtained molybdate-based inorganic–organic hybrid disks at 550 °C in air led to formation of orthorhombic α-MoO_3 nanoplates. X-ray diffraction (XRD), scanning electron microscopy (SEM), transmission electron microscopy (TEM), thermal analysis (TG–DTA), Fourier-transform infrared (FT–IR) spectra, Raman spectra, and a laser-diffraction grain-size analyzer were used to characterize the starting materials, the intermediate hybrid precursors and the final α-MoO_3 nanoplates. The XRD, FT–IR and TG–DTA results suggested that the molybdate-based inorganic–organic hybrid compound, with a possible composition of $(C_8H_{17}NH_3)_2MoO_4$, was of a highly ordered lamellar structure with an interlayer distance of 2.306(1) nm, and the *n*-alkyl chains in the interlayer places took a double-layer arrangement with a tilt angle of 51° against the inorganic MoO_6 octahedra layers. The SEM images indicated that the molybdate-based inorganic–organic hybrids took on a well-dispersed disk-like morphology, which differed distinctly from the severely aggregated morphology of their starting $MoO_3 \cdot H_2O$ powders. During the calcining process, the disk-like morphology of the hybrid compounds was well inherited into the orthorhombic α-MoO_3 nanocrystals, showing a definite plate-like shape. The α-MoO_3 nanoplates obtained were of a single-crystalline structure, with a side-length of 1–2 μm and a thickness of several nanometres, along a thickness direction of [010]. The above α-MoO_3 nanoplates were of a loose aggregating texture and high dispersibility. The chemical sensors derived from the as-obtained α-MoO_3 nanoplates showed an enhanced and selective gas-sensing performance towards ethanol vapors. The α-MoO_3 nanoplate sensors reached a high sensitivity of 44–58 for an 800 ppm ethanol vapor operating at 260–400 °C, and their response times were less than 15 s.

1. Introduction

Molybdenum trioxides (MoO_3) are important transition metal oxide semiconductors with unique functional properties.[1] Nanostructured MoO_3 materials have been intensively investigated and applied in smart windows,[2] gas sensors,[3–6] catalysts,[7–10] Li-ions batteries,[11–16] capacitors[17] and field emission devices.[18,19] There are basically two polytypic phases for MoO_3: one is the thermodynamically stable orthorhombic MoO_3 (α-MoO_3) phase, an n-type semiconductor with a wide band gap of 3.2 eV,[20] and the other is the metastable monoclinic MoO_3 (β-MoO_3) phase with a ReO_3-type structure.[2,12] The α-MoO_3 phase is of an anisotropic structure with layers parallel to the (010) crystal plane.[12] Each layer consists of two sublayers, and each sublayer is formed by corner-sharing octahedra along the [001] and [100] directions.[12] The two sublayers then stack together by sharing the edges of the octahedra along the [001] direction to form a layer.[6,12] These layers then alternately stack along the [010]

[a]*School of Materials Science and Engineering, Zhengzhou University, 100 Science Road, Zhengzhou, 450001, P. R. China. E-mail: dlchen@zzu.edu.cn*
[b]*School of Physics and Engineering, Zhengzhou University, 100 Science Road, Zhengzhou, 450001, P. R. China*
[c]*Laboratory of Aeronautical Composites, Zhengzhou Institutes of Aeronautical Industry Management, University Centre, Zhengdong New District, Zhengzhou, 450046, P. R. China*
[d]*School of Materials Science and Engineering, Henan University of Technology, 195 Zhongyuan West Road, Zhengzhou, 450007, P. R. China*
[e]*The State Key Laboratory of High Performance Ceramics and Superfine Microstructure, Shanghai Institute of Ceramics, Chinese Academy of Sciences, 1295 Dingxi Road, Shanghai, 200050, P. R. China*

† Electronic supplementary information (ESI) available: Comparison of $I_{(0k0)}/I_{(111)}$ values of the as-obtained α-MoO_3 nanocrystals and the literature data (JCPDS card No. 05-0508) on the basis of XRD results; the laser diffraction size-distribution curve of the as-obtained α-MoO_3 nanoplates. See DOI: 10.1039/c1jm11447f

‡ Present address: Institute of Metal Research, Chinese Academy of Sciences, 72 Wenhua Road, Shenyang 110016, P.R. China

direction to form an α-MoO_3 structure, where a van der Waals interaction is the major binding force between the MoO_6 octahedra layers.[6,12] The intrinsic structural anisotropy makes α-MoO_3 have abundant morphologies in nanostructures and can be used as host materials for intercalation applications.[11,12]

Recently, there have been a number of processes developed to synthesize MoO_3 nanocrystals with controlled shapes and sizes.[21–24] Nanobelts,[2,12,16,25–28] nanoribbons,[9] nanorods,[29–32] nanofibers,[33,34] nanoplatelets/nanosheets,[35–38] nanowires,[39,40] nanowiskers,[41] nanoflakes,[42] comb-like nanostructures,[43] nanotubes[44,45] and mesoporous nano-walls[17] have been successfully prepared using various technologies, including conventional hydrothermal processes,[9,12,26,33,34,46] thermal evaporation,[18,27,28] mechanical exfoliation,[36] atmospheric microplasma deposition,[37] growth from supercooled liquid nanodroplets,[40] cluster-based self-assembly routes,[43–45] template directed hydrothermal synthesis,[29] microwave-assisted hydrothermal reaction,[39] sonochemical process,[41] RF magnetron sputtering,[32] pyrolysis of organometallic precursors,[24,38] surfactant assisted hydrothermal processes,[16,31] and volumetric flame synthesis.[47] In general, most of these synthetic methods are captious and complex, and difficult to meet the requirements for large-scale synthesis and cost-effective applications.

Molybdate-based layered hybrids derived by intercalating organic guest species into the interlayer spaces of MoO_6 layers have also been a hot research topic,[48–55] and the as-obtained organic–inorganic hybrids can be used as the precursors to prepare MoO_3 nanostructures.[51,52,54,56,57] Mahjoub *et al.*[51] synthesized molybdenum oxide nanohybrids using yellow molybdic acid and amino-carboxylates as the starting materials in an ethanol-water (1 : 3) mixed solution, and α-MoO_3 nanostructures with high surface areas were obtained by calcining the as-obtained nanohybrids at 600 °C. Niederberger *et al.*[52] prepared molybdenum oxide-amine hybrid composites by hydrothermally treating the ethanol-water mixed suspension of yellow $MoO_3 \cdot 2H_2O$ and amines at 120 °C, and the molybdenum oxide-amine hybrid composites were used as the precursor to synthesize α-$MoO_3 \cdot H_2O$ nanofibers. Shao *et al.*[54] synthesized lamellar carboxymethyl cellulose (CMC)/molybdenum oxide hybrids, which were calculated at 500 °C to form uniform α-MoO_3 nanoplates. Shukoor *et al.*[57] systematically investigated the intercalation behaviors of amines with various *n*-alkyl lengths into yellow molybdic acid ($MoO_3 \cdot 2H_2O$) in ethanol/water (1/3, v/v) solutions, and the as-obtained hybrids were transformed to MoO_3 rods, scrolls and disks by 33% HNO_3 treatment. In these intercalation reactions, elevated temperatures are usually necessary.[52,55]

Transition metal semiconductor chemical sensors have wide applications in industrial and environmental aspects.[58–63] Nanostructures of SnO_2, WO_3 and $Cr_{2-x}Ti_xO_3$ (CTO) are the typical sensing materials to ethanol and other organic vapors.[58–63] Sensitivities and response rates can be adjusted by controlling the crystal sizes, shapes, compositions and thicknesses of the sensing material layers, but their selectivity to various types vapors are usually difficult to control.[58–62,64] To improve the discriminating ability, scientists have to develop novel materials or nanostructures.[63]

In this work, we develop a novel route to synthesize α-MoO_3 nanoplates using molybdate-based inorganic–organic hybrids as the precursors, which are formed from the reaction of white molybdic acid ($MoO_3 \cdot H_2O$) powders and *n*-octylamine at room temperature, and we evaluate the sensing properties of the MoO_3-nanoplates-based sensors to the vapors of alcohols, acetone, benzene and formaldehyde. The effects of reaction solvents on the formation of molybdate-based inorganic–organic hybrids, and the compositions, microstructures and thermal stability of the as-obtained hybrids are investigated in some detail. The topochemical transformation from molybdate-based inorganic–organic hybrids to α-MoO_3 nanoplates, and the related mechanisms for the gas-sensing response of the α-MoO_3 sensors are also discussed.

2. Experimental

2.1 Synthesis of molybdate-based hybrid disks and α-MoO_3 nanoplates

White molybdic acid ($MoO_3 \cdot H_2O$, Tianjin No.4 Chemical Reagent Factory, China), ethanol (CH_3CH_2OH, Tianjin Huadong Reagent Factory, China), heptane ($CH_3(CH_2)_5CH_3$, Tianjin Huadong Reagent Factory, China), and nitric acid (HNO_3, Kaifeng Fangjing Chemical Reagent Factory, China) were analytically pure. *n*-Octylamine ($C_8H_{17}NH_2$, chemically pure) was purchased from Beijing Chemical Reagent Co., Ltd. All of the reagents were used as purchased without any further purification. Distilled water was used in all the experiments.

$MoO_3 \cdot H_2O$ powders reacted with *n*-octylamine at room temperature to form molybdate-based inorganic–organic hybrid compounds. In a typical synthetic process, 10.3 mL of *n*-octylamine was firstly mixed with 113.7 mL of ethanol in a conical flask under magnetic stirring, and then 5.0 g of $MoO_3 \cdot H_2O$ powders was dispersed into the above mixture to form a white suspension. The as-obtained suspension was kept stirring for 72 h at room temperature in air, and a white mushy mixture was finally obtained. The white solids were collected by centrifugation, followed by washing with ethanol three times. The as-obtained solids were then air-dried at room temperature in a reduced pressure for more than 3 days, and 8.1 g of white powder, a molybdate-based inorganic–organic hybrid compound, was obtained. The molar ratios of *n*-octylamine to $MoO_3 \cdot H_2O$ were 2–10. The volume ratios of ethanol to *n*-octylamine were higher than 10. For the purpose of investigating the effects of reaction solvents on the formation of molybdate-based inorganic–organic hybrids, heptane, water and the mixture of ethanol/water (1 : 1 in volume) were used as the reaction solvents, respectively, to conduct the above experiments under a similar condition.

The as-obtained molybdate-based inorganic–organic hybrid compound was used as the precursor to prepare MoO_3 nanoplates. Typically, 2.0 g of the molybdate-based inorganic–organic hybrid compound was placed in an alumina crucible, which was then put into an electric furnace and kept at 550 °C for 1 h. After naturally cooling down to room temperature, about 1.0 g of gray powder was obtained. For the purpose of comparison, MoO_3 nanocrystals were also synthesized by calcining commercially available $MoO_3 \cdot H_2O$ powders at 550 °C for 1 h in air.

2.2 Characterization of molybdate-based hybrid disks and α-MoO_3 nanoplates

The phase compositions were identified by an X-ray diffraction (XRD) equipment (PANalytical X'Pert Pro, Holland) with a Cu-Kα radiation (λ = 1.5406 Å) under a voltage of 40 kV and a current of 40 mA. The XRD patterns were recorded with a speed of 0.02° s^{-1}. The scanning 2θ range for the molybdate-based inorganic–organic hybrid compound was 1.5–40°, while the scanning 2θ range was 10–60° for other samples. The morphologies were observed on a scanning electron microscope (SEM, FEI Quanta-200, Holland), with an EDX equipment (Amatek Edax Inc.). TEM images, HRTEM images, and SAED patterns were recorded on a Tecnai-G20 transmission electron microscope with an acceleration voltage of 200 kV. TG–DTA curves of the molybdate-based inorganic–organic hybrid compound were recorded on a thermal analysis system (WCT–2C, China) from room temperature to 850 °C with a heating rate of 5 °C min^{-1} in an air flow. Fourier-transform infrared (FT–IR) spectra of the molybdate-based inorganic–organic hybrid compound was recorded on an FT–IR spectrometer (Nicolet 460, USA) using the KBr disk technique. The Raman spectra of the MoO_3 nanoplates were recorded on a laser Raman spectroscope (LabRAM HR800) at room temperature. The grain-size distribution of the calcined powders was analyzed using a laser diffraction system (Malvern Mastersizer 2000, UK).

2.3 Fabrication of molybdenum trioxide nanoplate sensors

The fabrication of α-MoO_3 nanoplate sensors was similar to the previously reported process.[58] The as-obtained α-MoO_3 nanoplates were mixed with a small amount of ethanol to form an α-MoO_3 paste, which was then brush-coated onto the surfaces of an Al_2O_3 microtube with four Pt electrodes. After the α-MoO_3 coating was air-dried, the coating process was repeated until a complete coating was formed. The α-MoO_3-coated Al_2O_3 microtube was then fixed to a special pedestal with 6 poles by welding the four Pt electrodes to 4 poles of the pedestal, respectively. A heating coil was then inserted through the Al_2O_3 microtube and its two ends were welded to the other two poles of the pedestal.

2.4 Measurement of gas sensing properties of molybdenum trioxide nanoplate sensors

The gas sensing properties of α-MoO_3 nanoplate sensors were tested using a commercial computer-controlled WS-30A system under a static testing condition. Various vapors (*e.g.*, methanol, ethanol, isopropanol, acetone, formaldehyde and benzene) were used as the target gases to characterize the sensing performance of the α-MoO_3 sensors. The concentrations of the target gases were 5–800 ppm, calculated according to the densities and the volume of the testing chamber. Liquid reagents were injected into a hot stage located in the chamber, and then they were evaporated quickly to form the corresponding vapors. The vapor concentrations (2–800 ppm) were calculated according to the densities of the liquid reagents and the volume of the chamber. The amounts (V_{tg}, μL) of the target reagents are determined according to eqn (1).

$$V_{tg} = \frac{10^{-9} V_0 \cdot M \cdot C_{tg}}{22.4 \rho \cdot p} \quad (1)$$

Here, V_0 is the volume of the chamber (V_0 = 13.8 L), ρ is the density of the target liquid reagent (g cm^{-3}), M is the mole mass (g mol^{-1}) of the target liquid reagent, p is the rate of purity of the target liquid reagent, and C_{tg} is the concentration (ppm) of the target liquid reagent. The operating temperatures were 200–400 °C, controlled by an electric heating system. The relative humidity (RH) of the environment was 30–40%.

The α-MoO_3 sensor (R) was connected in series with a load resistor (R_0) with a known resistance, and a source voltage (U_0) of 5 V was loaded on the circuit, which was similar to the previous report.[58] The system measured the voltages (U) loaded on the resistor R_0, and the resistances (R) of the α-MoO_3 sensors can therefore be calculated according to eqn (2). For the reducing gases and n-type semiconducting α-MoO_3 sensors, the sensitivity (S_r) is defined as eqn (3), where R_a and R_g are the resistances of the α-MoO_3 sensor in ambient air and in ambient gases, respectively. The response time (T_{res}) is defined as the time required for the sensor to reach 90% of the stabilized value of its resistance in the presence of the test gas. Similarly, the recovery time (T_{rec}) is defined as the time required for the sensor to reach 10% of the initial steady state value of its resistance after the gas was removed.

$$R = \frac{U_0 - U}{U} \times R_0 \quad (2)$$

$$S_r = R_a / R_g \quad (3)$$

3. Results and disscussion

3.1 Morphologies and microstructures of molybdate-based inorganic–organic hybrid disks

Fig. 1(a)–(b) shows the XRD patterns of the $MoO_3 \cdot H_2O$ and the resultant hybrid compound by a reaction of $MoO_3 \cdot H_2O$ with *n*-octylamine in ethanol. As Fig. 1(a) shows, there are a series of intense diffraction peaks at 2θ = 12.35°, 14.82°, 18.52°, 22.03°, 24.83°, 27.04°, 30.29°, *etc.* When we refer to the JCPDS cards, it is difficult to determine what phases the sample is composed of according to the known literature data. The commercial $MoO_3 \cdot H_2O$ may be a mixture of intermediate phases of molybdic acids with a certain amount of crystal water. Fig. 1(b) shows the XRD pattern of the product of the above commercial molybdic acid reacting with *n*-octylamine in ethanol at room temperature, with a molar ratio of molybdic acid to *n*-octylamine of 1 : 5 (n_{Mo}:n_N = 1 : 5). There are 4 highly intense diffraction peaks with regularly reduced intensities in the low 2θ-angle range of 1.5–20°, indicating that the as-obtained product is of a highly ordered layered structure. The newly formed peaks are located at 2θ = 3.836°, 7.671°, 11.507°, and 15.342°, which can be indexed to the reflections from (010), (020), (030) and (040) diffraction planes, respectively, when considering the layered structure of MoO_3 along the *b*-axis direction. The interlayer distance (d) can be calculated to be d = 2.306(1) nm using a program UnitCell, refined in a cubic system (λ = 1.54055 Å) by minimizing the sum of squares of

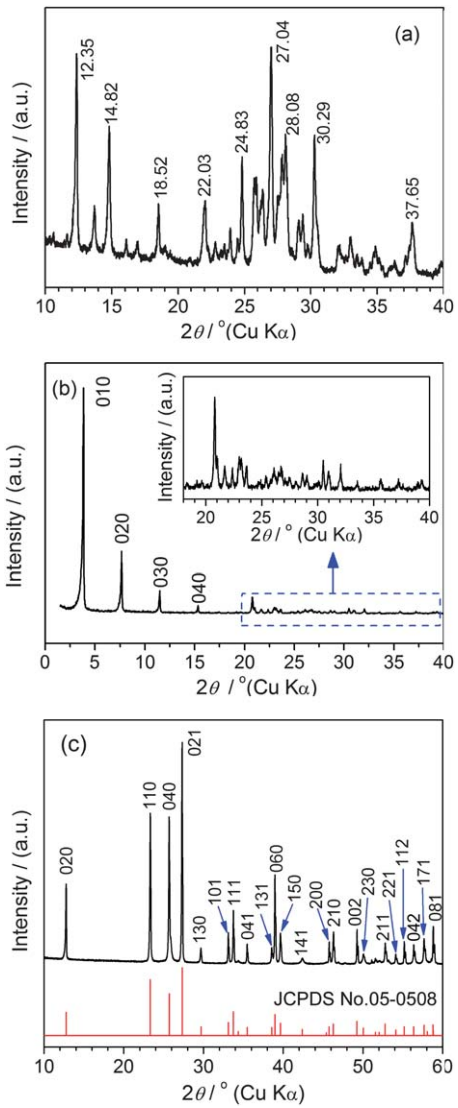

Fig. 1 XRD patterns of (a) commercial molybdic acid; (b) molybdate-based inorganic–organic hybrid compound derived from the reaction of commercial molybdic acid with *n*-octylamine in ethanol (n_{Mo}:n_N = 1 : 5); (c) MoO_3 nanocrystals derived by calcining the molybdate-based hybrid compound at 550 °C (the inset is the data from JCPDS card No. 05–0508).

residuals in 2θ. In the 2θ-angle range of 20°–40°, there are numerous diffraction peaks with low intensities, as shown as the inset of Fig. 1(b). These diffraction peaks are similar to those of molybdic acid (Fig. 1(a)), and can mainly be attributed to the reflections from the inorganic MoO_6 frames.

Fig. 2 shows the SEM images of the commercial molybdic acid and the resultant molybdate-based hybrid compound obtained with n_{Mo}:n_N = 1 : 5. As Fig. 2(a)–(b) show, the commercial molybdic acid consists of large aggregates with sizes of 10–15 μm, and the original grains are platelike particles with side sizes of 1–3 μm. These platelike particles are assembled tightly together to form spherical/rodlike aggregates, as shown as Fig. 2(a)–(b). Fig. 2(c)–(d) show the morphology of the product derived from the reaction of commercial molybdic acid with *n*-octylamine in ethanol. The product consists of separate disklike particles. The

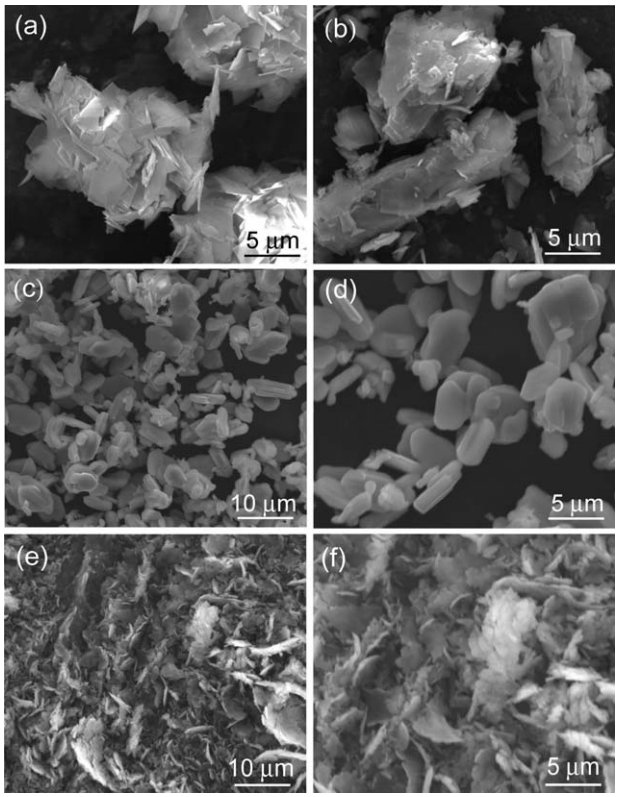

Fig. 2 SEM images of (a, b) commercial molybdic acid; (c, d) molybdate-based hybrid compound derived from the reaction of commercial molybdic acid with *n*-octylamine in ethanol (n_{Mo}:n_N = 1 : 5); and (e, f) α-MoO_3 nanocrystals derived by calcining the molybdate-based hybrid compound at 550 °C for 1 h in air.

thicknesses of the disks are 1.55 ± 0.4 μm, and the apparent side sizes are 5.2 ± 1.7 μm, according to the SEM observations. The average side-to-thickness ratio of the as-obtained disks is 3.5. When comparing Fig. 2(a)–(b) and Fig. 2(c)–(d), one can readily find that the morphology of the as-obtained product is completely different from that of its starting material of commercial molybdic acid, not only in size but also in shape, indicating a recrystallization and reorganization process has occurred during the reaction of molybdic acid with *n*-octylamine in ethanol.

The structure of the as-obtained disks from the reaction of molybdic acid and *n*-octylamine are characterized by the FT–IR spectrum, as shown as Fig. 3. The bands in the 500–1000 cm^{-1} region are due to Mo–O stretching modes.[32] The absorption band at 905 cm^{-1} is attributed to the stretching vibration of $Mo{=}O_{terminal}$, moving towards the low-frequency region.[12,51,56] The absorption band at 850 cm^{-1} is assigned to the doubly coordinated oxygen (Mo_2–O) stretching mode which results from the corner-shared oxygen in common with two MoO_6 octahedra, and the band at 590 cm^{-1} is assigned to the triply coordinated oxygen (Mo_3–O) stretching mode which results from the edge-shared oxygen in common with three MoO_6 octahedra.[12,32,51,56] The bands in the region of 2800–3000 cm^{-1} are assigned to the C–H stretching modes of the polymethylene [–$(CH_2)_n$–] chains (2857 cm^{-1}, ν_s (CH_2); 2917 cm^{-1}, ν_{as} (CH_2)) and end-methyl (–CH_3) groups (2960 cm^{-1}, ν_{as} (CH_3)).[65] The

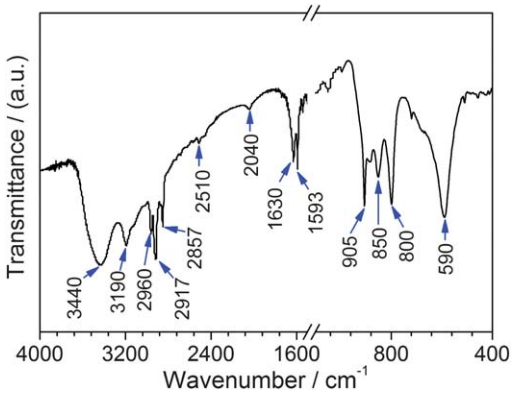

Fig. 3 A typical FT–IR spectrum of the molybdate-based hybrid compound derived from the reaction of commercial molybdic acid with *n*-octylamine in ethanol (n_{Mo}:n_N = 1 : 5).

band at around 3190 cm^{-1} is assigned to the stretching vibration of the N–H group. The weak bands near 2510 cm^{-1} are assignable to the symmetric stretching modes of NH_3^+ groups.[57] The bands at 1630 and 1593 cm^{-1} correspond to the bending vibrations of N–H and O–H, respectively.[57] The band at 3440 cm^{-1} can be assigned to the ν(O–H) stretching mode of adsorbed water molecules. A broad band at around 2040 cm^{-1} is due to a combination of the asymmetrical bending vibration and torsional oscillation of the $-NH_3^+$ groups interacting with the apical oxygen of the Mo–O framework, *i.e.* $R–NH_3^+\cdots{}^-O–Mo$, which is similar to the case of tungstate-based hybrid compounds.[65] The FT–IR results confirm the existence of the inorganic layers of Mo–O frames and organic layers of *n*-alkylammonium ions ($R–NH_3^+$). Furthermore, the inorganic layers of Mo–O frames and the organic layers of *n*-alkylammonium ions ($R–NH_3^+$) have point-specific interaction, forming weak chemical bonds. When considering the FT–IR results together with the XRD results and the reaction conditions, one can safely conclude that the disks obtained by reacting molybdic acid with *n*-octylamine in ethanol is a molybdate-based inorganic–organic hybrid compound with a highly ordered layered structure, alternately consisting of inorganic Mo–O layers and organic *n*-alkylammonium ions along the [010] direction when referring to the orthorhombic MoO_3 structure.[57,65]

The thermal analytical results of the inorganic–organic hybrid disks obtained are shown in Fig. 4. Fig. 4(a) shows the TG curve of the molybdate-based inorganic–organic hybrid compound at 20–900 °C. As the TG curve shows, there are four obvious mass-loss stages: (I) 20–210 °C with a mass loss of 28%, (II) 210–340 °C with a mass loss of 11%, (III) 340–550 °C with a mass loss of 28%, and (IV) 700–900 °C with a mass loss of 27%. Fig. 4(b) shows the corresponding DTA result. In stage I, there are two weak endothermic peaks at 136 °C and 185 °C, which are due to desorption of *n*-octylammonium ions/molecules and the decomposition of crystal water in the Mo–O frames, respectively. The corresponding mass loss of 28% attributes to the removal of the adsorbed *n*-octylammonium ions/molecules and crystal water. In stage II, there is two strong exothermal peaks at around 249 and 280 °C, respectively, which should be attributed to the oxidization of the organic $-(CH_2)_n-$ chains in the hybrid compound. The corresponding mass loss (11%) is due to the

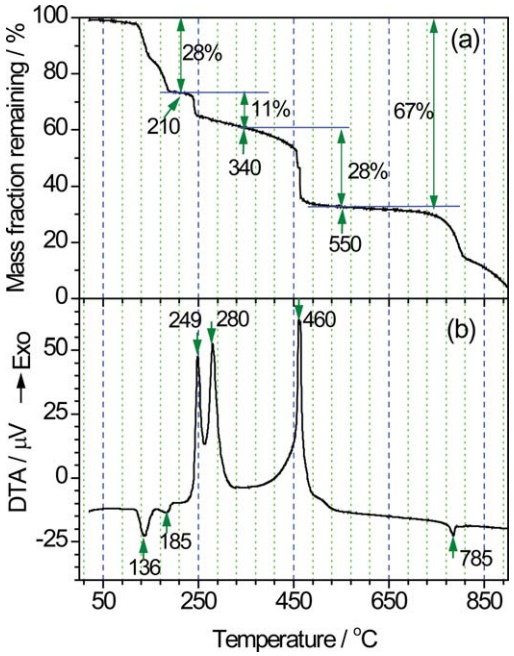

Fig. 4 (a) TG and (b) DTA curves of the molybdate-based hybrid compound obtained from the reaction of commercial molybdic acid with *n*-octylamine in ethanol (n_{Mo}:n_N = 1 : 5).

release of small volatile molecules resulting from the oxidization of long *n*-alkyl chains. The resultant inorganic carbon species formed in stage II then combusts at elevated temperatures of 340–550 °C, confirmed by the strong exothermal peak at 460 °C, and the mass loss of 28% in stage III. Over the temperature range of 550–700 °C, there are no detectable changes either in the TG curve or in the DTA curve, indicating that a thermally stable α-MoO_3 phase is formed. When the temperature is higher than 700 °C, *i.e.*, stage IV, there is a weak endothermic peak at around 786 °C, accompanied by a mass loss of 33%. It is the melting and then evaporating behavior of MoO_3 that accounts for the endothermic peak and the large mass loss in stage IV. The total mass loss at 20–520 °C is 67%. If the composition of the molybdate-based inorganic–organic hybrid compound can be expressed as $(C_8H_{17}NH_3)_xH_{2-x}MoO_4$, and the product calcined at a temperature higher than 550 °C is MoO_3, the *x* value can be calculated to be about 2.12 according to the mass loss (67%). Therefore, the composition of the molybdate-based inorganic–organic hybrid compound can be described as $(C_8H_{17}NH_3)_2MoO_4$. According to $MoO_3\cdot H_2O + 2C_8H_{17}NH_2 \rightarrow (C_8H_{17}NH_3)_2MoO_4$, 5.0 g of $MoO_3\cdot H_2O$ powders can theoretically produce 9.24 g of $(C_8H_{17}NH_3)_2MoO_4$. Actually, about 8.1 g of such hybrid was obtained in the experiment, and the productive rate is 88%, which is reasonable when considering the loss during the experimental procedure.

3.2 Morphologies and microstructures of α-MoO_3 nanoplates

Fig. 1(c) shows the XRD pattern of the product obtained by calcining the molybdate-based inorganic–organic hybrid disks at 550 °C for 1 h in air. As Fig. 1(c) shows, all the diffraction peaks can be readily indexed to an orthorhombic MoO_3 phase (α-MoO_3, space group: Pbnm (62)) according to JCPDS card

No. 05–0508, as shown as the inset of Fig. 1(c). The calculated cell parameters by refining the XRD pattern on the basis of the principle by minimizing the sum of squares of residuals in 2θ are $a = 3.964(2)$ Å, $b = 13.862(3)$ Å and $c = 3.6991(8)$ Å, which are close to the literature data ($a = 3.962$ Å, $b = 13.858$ Å, $c = 3.697$ Å, JCPDS card No. 05–0508). The ratios of $I_{(0k0)}$ to $I_{(111)}$ of the as-obtained α-MoO_3 and the literature data (JCPDS card No. 05–0508) are listed in Table 1. One can easily find that the $I_{(0k0)}I_{(111)}$ values of the as-obtained α-MoO_3 are obviously larger than those of the literature data, indicating that the as-obtained α-MoO_3 sample is of an obvious preferred orientation growth along the (0k0) planes. In other words, the (0k0) planes have the largest probability to be exposed to the environment. The preferred orientation growth may be attributed to the synthetic method by using a molybdate-based inorganic–organic hybrid compound with a layered structure along the (0k0) planes as the starting material.

Fig. 2(e)–(f) show the SEM images of the α-MoO_3 sample derived by calcining the molybdate-based inorganic–organic hybrid disks at 550 °C for 1 h in air. The SEM images with various magnifications suggest that the α-MoO_3 sample is composed of platelike nanocrystals with a good dispersibility in a large view field (Fig. 2(e)). As Fig. 2(e)–(f) show, the platelike particles are of side sizes of 1–10 μm and thicknesses of 50–150 nm. The platelike morphology of the as-obtained α-MoO_3 sample makes them tend to lie down along a substrate with their large surfaces parallel to the substrate, because of their large side-to-thickness ratios. Considering the preferred growth of the (0k0) planes together with their platelike morphology, one can safely conclude that the as-obtained α-MoO_3 nanoplates have a shortest side along the b-axis, that is, the thickness of the α-MoO_3 nanoplates is along the b-axis (*i.e.*, the [0k0] direction). The laser-diffraction size-distribution curve (Fig. S1)† of the as-obtained α-MoO_3 nanoplates suggests that the apparent size range is 1.0–22.5 μm, with a peak value of 5.0 μm. The sizes from laser diffraction are larger than those from the SEM observations (Fig. 2(e)–(f)), which is probably due to the overlap joint of the α-MoO_3 nanoplates in the ethanol suspension.

Fig. 5 shows the typical TEM observations of the α-MoO_3 nanoplates obtained by calcining the molybdate-based inorganic–organic hybrid disks at 550 °C for 1 h in air. As the low-magnification TEM image in Fig. 5(a) shows, most of the α-MoO_3 nanoplates take on a quadrilateral platelike shape with a lateral length of 1–2 μm. Also, one can find that some α-MoO_3 nanoplates are partially overlapped with each other, agreeing with the SEM observations (Fig. 2(f)). Fig. 5(b) shows a typical individual α-MoO_3 nanoplate with a dimension of 1000 nm × 600 nm and its thickness is very thin (several nanometres) judged by the shallow contrast grade. Fig. 5(c) shows a typical SAED pattern of the individual α-MoO_3 nanoplate shown in Fig. 5(b). As Fig. 5(c) shows, it is composed of a highly-ordered diffractional lattice with a large and homogeneous diffraction dot array, which suggests that the α-MoO_3 nanoplate is of a single-crystal structure and has a thin and uniform thickness. The SAED pattern can be indexed to an orthorhombic α-MoO_3 phase with a zone axis along the [010] direction. Fig. 5(d) shows an HRTEM image of an edge of the α-MoO_3 nanoplate shown in Fig. 5(b), the two-dimensional lattice stripes of which indicate that the α-MoO_3 nanoplate is single-crystal. The distances of lattice

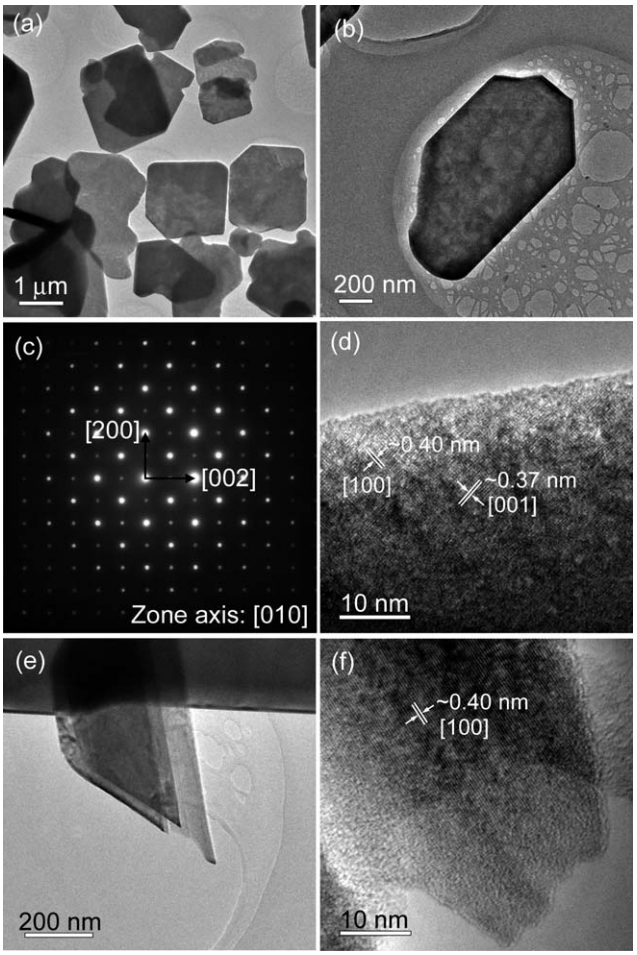

Fig. 5 (a) A low-magnification TEM image of α-MoO_3 nanoplates; (b) a TEM image, (c) an SAED pattern and (d) an HRTEM image of an individual α-MoO_3 nanoplate; (d) a TEM image of laminated α-MoO_3 nanoplates, and (f) an HRTEM image of the tip of an α-MoO_3 nanoplate.

stripes are about 0.40 nm and 0.37 nm, corresponding to the (100) and (001) planes of the α-MoO_3 phase, respectively. The HRTEM observation agrees with its SAED pattern very well.

The as-obtained α-MoO_3 nanoplates may consist of thinner sub-plates because of the formation process on the basis of interaction chemistry. Fig. 5(e) shows a typical example. The α-MoO_3 nanoplate is composed of three super-thin subplates, which overlap loosely with each other. Fig. 5(f) shows an HRTEM image of a tip of one of the subplates, and the clear lattice stripes indicate that the sub-plate is also of a well-defined single-crystal structure.

Fig. 6 shows a typical EDX pattern of the α-MoO_3 nanoplates derived by calcining molybdate-based inorganic–organic hybrid disks at 550 °C in air. As Fig. 6 shows, the sample consists of two elements, *i.e.*, Mo and O, without any other impurities. The atomic ratio of O to W is about 2.65, very close to the stoichiometric proportion (3) for the α-MoO_3 phase.

A typical Raman spectrum of the α-MoO_3 nanoplates is shown in Fig. 7, the inset of which shows the atomic arrangement of a [MoO_6] octahedron in the α-MoO_3 phase.[66,67] The vibration modes appearing in the frequency ranges of 1000–600 cm^{-1} and 600–200 cm^{-1} correspond to the stretching and deformation

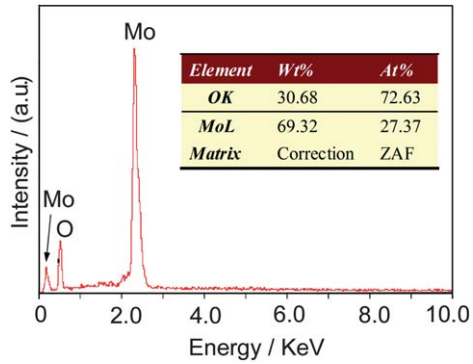

Fig. 6 EDX pattern of α-MoO_3 nanoplates derived from molybdate-based inorganic–organic hybrid disks.

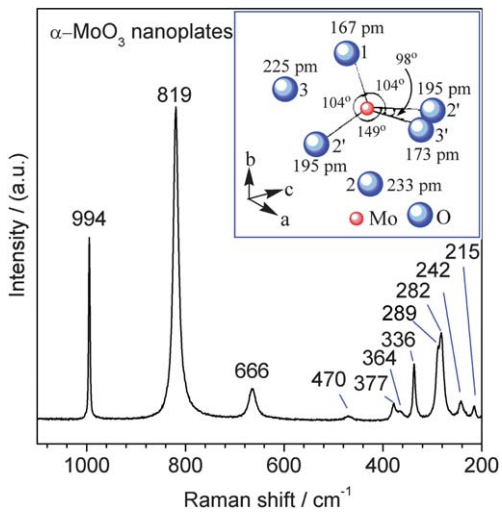

Fig. 7 Raman spectrum of α-MoO_3 nanoplates derived from molybdate-based inorganic–organic hybrid disks.

modes, respectively.[66,68,69] The narrow band at 994 cm^{-1} is assignable to the antisymmetric ν(Mo=O_1) stretching (A_g), in which the bonding aligns along the *b* axis direction.[67–70] The strong band at 819 cm^{-1} represents the symmetric ν(Mo–O_3–Mo) stretching (A_g) with the bonding aligning along the *a* axis direction.[67–69] The weak and broad bands at 666 and 470 cm^{-1} are ascribable to the antisymmetric ν(Mo–O_2–Mo) stretching (B_{2g}) and bending (A_g), respectively.[67–69] The bands at 377 and 364 cm^{-1} correspond to the δ(O_2=Mo=O_2) scissor (B_{1g} and A_g modes).[67–69] The band at 336 cm^{-1} is characteristic of the δ(O_3–Mo–O_3) deformation (B_{1g}).[67–69] The band at 282 cm^{-1} and a weak shoulder centered at 289 cm^{-1} correspond to the δ(O_1=Mo=O_1) wagging (B_{2g} and B_{3g}, respectively).[66–69] The bands at 242 and 215 cm^{-1} correspond to the δ(O_2–Mo–O_2) scissor (B_{3g} and A_g modes, respectively).[67–69]

3.3 Formation mechanisms of molybdate-based hybrid disks and α-MoO_3 nanoplates

The interaction of commercially available $MoO_3 \cdot H_2O$ and *n*-octylamine can be seen as an acid–base reaction. When water or ethanol/water were used as the reaction solvents, no solid products were obtained. This is because the formed molybdate can dissolve in highly alkaline solutions, which are formed *via* the hydrolysis of excess *n*-octylamine in a solvent containing water. When heptane was used as the reaction solvent, the reaction of $MoO_3 \cdot H_2O$ and *n*-octylamine was very slow, and there was no obvious change even after reacting for 2 weeks. When ethanol was used as the reaction solvent, a white milky suspension was formed in several hours.

Fig. 8 shows the schematic of the formation mechanisms for the molybdate-based inorganic–organic hybrid disks and the α-MoO_3 nanoplates. In the stage of A → B, molybdic acid reacts with *n*-octylamine *via* an acid–base mechanism, where an intercalation and reorganization process is undergone. The length of an *n*-octylamine molecule can be evaluated to be l_1 = 1.137 nm, according to the length (0.248 nm) of a CH_3NH_2 molecule and the length (0.127 nm) per –CH_2–. The contribution (l_0 = 1.756 nm) of the organic species to the interlayer distance can be calculated by subtracting the thickness (l_2 = 0.55 nm) of the double MoO_6 layer from the interlayer distance (l_3 = 2.306 nm). The thickness (l_0) of the organic species is larger than the length (l_1) of an *n*-octylamine molecule (or an *n*-octylammonium ion), and the *n*-octyl chains, therefore, take a double-layer arrangement with a tilt angle of $\alpha = \sin^{-1}(l_0/2l_1) = 51°$ (Fig. 6B), which is in good agreement with the previously reported result (50.8°).[55] The organic layers of molybdate-based inorganic–organic hybrid disks are removed by a thermal treating process at 550 °C and the platelike α-MoO_3 nanocrystals are obtained, as shown as the stage of B → C. The synthesis of α-MoO_3 nanoplates can be seen as a pseudo-topochemical transformation, where the platelike morphology is transferred from the precursors to the final products. The possible chemical reactions can be described as eqn (4)–(5).

$$MoO_3 \cdot H_2O(s) + C_8H_{17}NH_2(l) \xrightarrow{\text{r.t. \& in ethanol}} (C_8H_{17}NH_3)_2 MoO_4(s, \text{disks}) \quad (4)$$

$$(C_8H_{17}NH_3)_2MoO_4(s, \text{disks}) \xrightarrow{550°C \text{ in air}} MoO_3(s, \text{nanoplates}) + CO_2(g) + H_2O(g) + NH_3(g) \quad (5)$$

To demonstrate the role of the molybdate-based inorganic–organic hybrid precursors in the formation of α-MoO_3 nanoplates, we also synthesized α-MoO_3 nanocrystals by calcining commercially available $MoO_3 \cdot H_2O$ powders at 550 °C for 1 h in

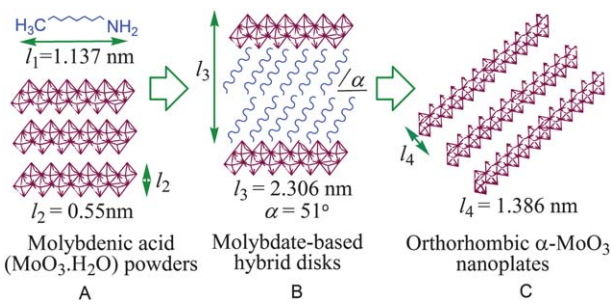

Fig. 8 A schematic of the formation mechanism for the molybdate-based inorganic–organic hybrid compound and the resultant α-MoO_3 nanoplates.

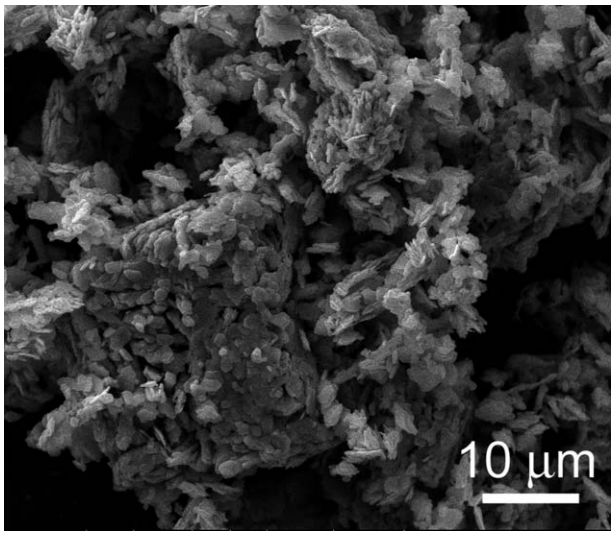

Fig. 9 SEM image of particulate MoO_3 nanocrystals derived by calcining commercial molybdic acid ($MoO_3 \cdot H_2O$) at 550 °C for 1 h in air.

air. Fig. 9 shows a typical SEM image of the as-obtained α-MoO_3 product from $MoO_3 \cdot H_2O$ powders. One can find that particulate shapes are the dominant morphology for the α-MoO_3 sample obtained directly from $MoO_3 \cdot H_2O$ powders. In addition, most of the α-MoO_3 particles are conglutinated to form large agglomerates. This comparative investigation indicates that molybdate-based inorganic–organic hybrid disks are necessary in the formation of single-crystal α-MoO_3 nanoplates with a large diameter-to-thickness ratio.

3.4 Gas-sensing performance of the α-MoO_3 nanoplate sensors

The as-obtained α-MoO_3 nanoplates are used as the sensitive material to fabricate chemical sensors, the gas-sensing properties of which are evaluated using various volatile reagents as the target substances, including ethanol, methanol, isopropanol, formaldehyde, acetone and benzene. Fig. 10 shows the typical response profiles to various vapors with concentrations of 5–800 ppm at operating temperatures of 260–400 °C. When the operating temperature is 260 °C, the α-MoO_3 nanoplate sensors show an obvious response to ethanol and methanol vapors, whereas there is almost no response for the vapors of isopropanol, formaldehyde, acetone and benzene, as shown as Fig. 10(a). As the operating temperature increases from 260 to 300 °C, the response peaks to ethanol and acetone vapors are improved to some extent, but the response to methanol vapors becomes obviously weaker, as shown as Fig. 10(b). At an operating temperature of 350 °C, as shown in Fig. 10(c), the α-MoO_3 nanoplate sensors show an obvious response to the vapors of methanol, acetone, isopropanol, formaldehyde and benzene, but their signals are still much weaker than those of ethanol vapors with different concentrations. When the operating temperature is up to 400 °C, as shown an Fig. 10(d), the response signal intensities of the α-MoO_3 nanoplate sensors are divided into three zones: the ethanol vapors have the strongest sensing signals, the vapors of methanol and acetone show the second strongest sensing signals, and the vapors of isopropanol, formaldehyde and benzene show the weakest sensing signals.

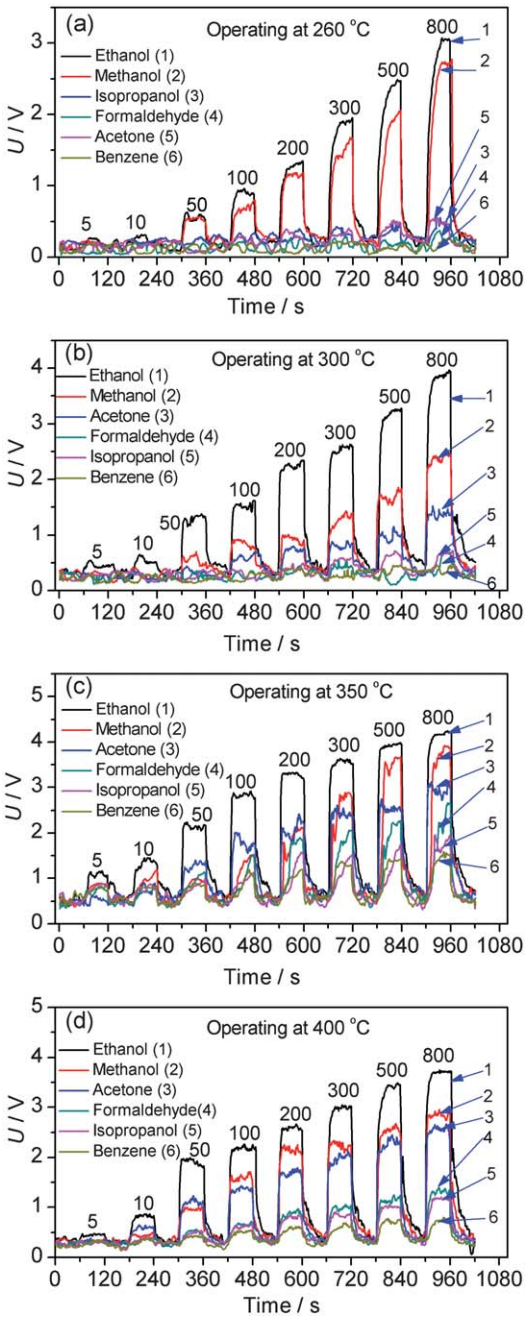

Fig. 10 Typical response profiles of the α-MoO_3 nanoplate sensors exposing to various reagent vapors with different concentrations operating at (a) 260 °C (R_0 = 20 MΩ), (b) 300 °C (R_0 = 20 MΩ), (c) 350 °C (R_0 = 20 MΩ), and (d) 400 °C (R_0 = 4.7 MΩ).

Fig. 11 shows the plots of the sensitivities of the α-MoO_3 nanoplate sensors as a function of the concentrations of different reagent vapors operating at 260–400 °C. As Fig. 11(a) shows, the sensitivities to ethanol vapors present a linearly increasing trend from 2 to 54 as the concentration of the ethanol vapor increases from 5 to 800 ppm, and a similar linear relationship is also seen for methanol vapors (4–34 for 50–800 ppm), when the operating temperature is 260 °C. When operated at 300 °C, the α-MoO_3 nanoplate sensors show similar high sensitivities to ethanol vapors (2–58 for 5–800 ppm), whereas their sensitivities to

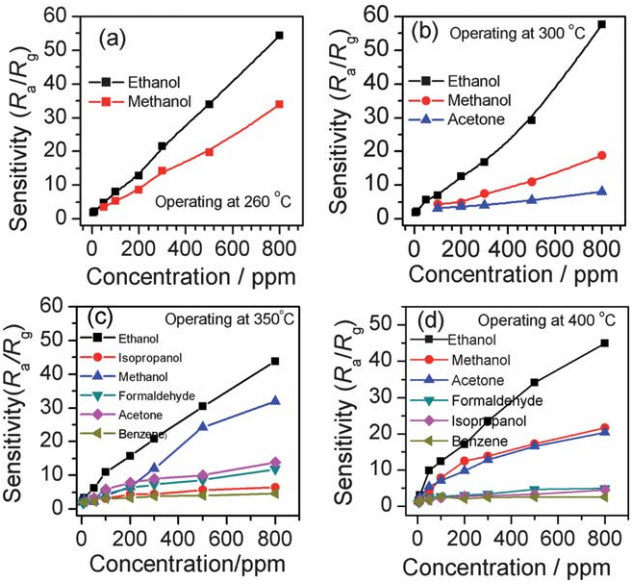

Fig. 11 The plots of the sensitivities of the α-MoO_3 nanoplate sensors as a function of the concentrations of different reagent vapors operating at (a) 260 °C (R_0 = 20 MΩ), (b) 300 °C (R_0 = 20 MΩ), (c) 350 °C (R_0 = 20 MΩ), and (d) 400 °C (R_0 = 4.7 MΩ).

methanol vapors are 4–19 for 50–800 ppm, lower than those (4–34 for 50–800 ppm) operated at 260 °C, as shown in Fig. 11(b). The sensitivities of the α-MoO_3 nanoplate sensors to acetone vapors shows a good linear increase with the increase in concentrations, but their sensitivities are less than 10 even at 800 ppm. For ethanol vapors, the sensitivities show a similar change trend when the operating temperature increases from 350 to 400 °C, and the sensitivity values increase from about 2 to 44 when the concentrations of ethanol vapors increase from 5 to 800 ppm. When the operating temperature is 400 °C, the sensitivities of isopropanol, formaldehyde and benzene vapors are very low (less than 5) in the concentration range of 5 –800 ppm, whereas the sensitivities are about 1.2–22 for 5–800 ppm of methanol and acetone vapors. When comparing Fig. 10 and Fig. 11, one can readily find that the α-MoO_3 nanoplate sensors obtained have the highest sensitivity to ethanol vapors, while for the vapors of benzene, isopropanol and formaldehyde, the α-MoO_3 nanoplate sensors show the lowest sensitivity in the operating temperature range of 260–400 °C. One can conclude that the α-MoO_3 nanoplate sensors show an obvious selectivity and that they have the highest sensitivity to ethanol vapors.

Fig. 12 shows the plots of the sensitivities of the α-MoO_3 nanoplate sensors to ethanol vapors *versus* the operating temperatures (260–400 °C). As the figure shows, the operating temperature has no obvious influence on the sensitivity in a low ethanol-concentration range of 5–200 ppm, whereas for 300–800 ppm ethanol vapors, the α-MoO_3 nanoplate sensors have higher values in sensitivity at 260 °C than those at 300–400 °C.

The response and recovery times of the α-MoO_3 nanoplate sensors to ethanol vapors with various concentrations are shown in Fig. 13. Generally, the response times of α-MoO_3 nanoplate sensors decrease with the increase in operating temperature, from 15–38 s at 260 °C to 7–14 s at 400 °C. However, the recovery times (*i.e.*, 10–40 s) almost show no obvious change in the

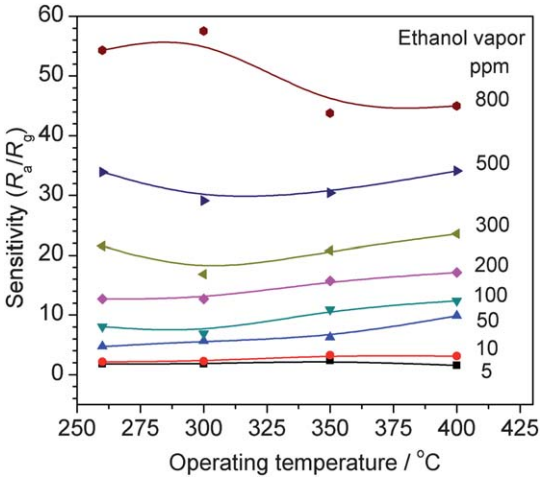

Fig. 12 The sensitivity changes of the α-MoO_3 nanoplate sensors at various operating temperatures under ethanol vapor with a concentration range of 5–800 ppm.

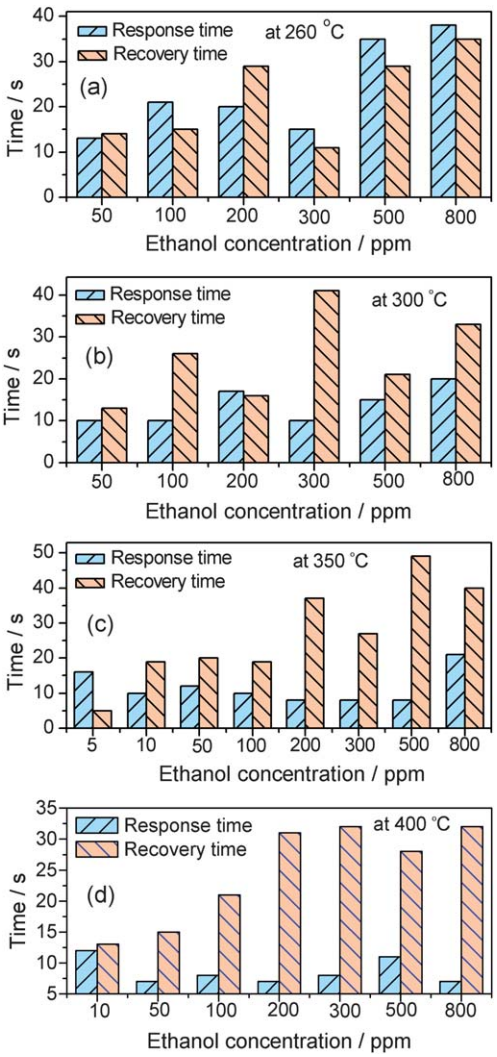

Fig. 13 The response and recovery times of the α-MoO_3 nanoplate sensors as a function of the ethanol concentrations operating at 400 °C (R_0 = 4.7 MΩ).

operating temperature range of 260–400 °C. The recovery time slightly increases with an increase in the concentration of ethanol vapors (Fig. 13(c)–(d)). The response times are almost comparable to other sensors made from SnO_2 and WO_3 nanocrystals.[59–64]

Comini *et al.*[4] have investigated the ethanol-sensing property of MoO_3 nanorods synthesized by infrared-irradiation heating of a Mo foil, and found that the MoO_3 nanorod sensors were sensitive to ethanol vapors (20–600 ppm) operating at 200 °C, but their sensitivities were less than 20. Glatasis *et al.*[71] have reported the ethanol-sensing property of MoO_3 nanocrystals obtained by a sol–gel process, and the sensitivity of 600 ppm ethanol operating at 300 °C was about 14. When comparing these literature data with the present results, one can find the α-MoO_3 nanoplate sensors reported here show an obviously enhanced ethanol-sensing performance. One can also find that the α-MoO_3 nanoplate sensors here show a good discrimination between ethanol and other organic vapors, as shown as Fig. 11(d) (*i.e.*, ethanol > methanol ≈ acetone > formaldehyde ≈ isopropanol ≈ benzene). The enhanced enthanol-sensing property and discriminating ability may be related to the single-crystalline structure and the plate-like morphology of the α-MoO_3 nanoplates, providing channels for rapid and effective diffusion of target vapors.

There are many other ethanol-sensing materials reported in the literature. Pratsinis *et al.*[59] reported a SnO_2-CuO ethanol-sensing sensor with a superhigh sensitivity (673 for a 100 ppm ethanol vapor at 320 °C) by optimizing the thickness of the bottom CuO layer. Wang *et al.*[60] reported a sensor made from Au-decorated SnO_2 hollow spheres, showing a high sensitivity of 220 for a 100 ppm ethanol vapor at 300 °C, with an obvious selectivity discrimination from acetone. Binions *et al.*[63] developed zeolite modified metal oxide semiconductor (WO_3 or CTO) gas sensors, and found that zeolite can improve the discrimination between ethanol and isopropyl alcohol. Blackman *et al.*[61] used Au-decorated WO_3 nanoneedles to fabricate sensors, which show some response to a low-concentration ethanol vapor (about 1.5 ppm) but with slow response speeds. We also reported a WO_3 nanoplate sensor for alcohol detection, but it showed obvious response to acetone at the same time.[56,64] One can conclude that the good discrimination of α-MoO_3 nanoplate sensors between ethanol and other organic vapors and their rapid response speeds are affirmative when we consider the simplicity and high-efficiency in the synthetic method of α-MoO_3 nanoplates, without any decorating substances, although the sensitivities and detecting concentrations of the α-MoO_3 nanoplate sensors to ethanol vapors do not surmount those of the SnO_2 and WO_3 sensors.

4. Conclusions

Molybdate-based inorganic–organic hybrid disks with a highly ordered lamellar structure have been synthesized *via* an acid–base reaction of white molybdic acid ($MoO_3 \cdot H_2O$) and *n*-octylamine in ethanol at room temperature. The interlayer distance of the as-obtained hybrid is 2.306(1) nm, and the *n*-alkyl chains in the interlayer places take a double arrangement with a tilt angle of 51°. The types of solvents have key effects on the formation of the molybdate-based inorganic–organic hybrids: water, a mixture of ethanol/water, and heptane are not favorable for the formation of ordered molybdate-based inorganic–organic lamellar hybrids. The thermal treatment of the as-obtained molybdate-based inorganic–organic hybrid disks at 550 °C resulted in the formation of orthorhombic α-MoO_3 nanoplates with a side-length of 1–2 μm and a thickness of several nanometres, along a thickness direction of [010]. The chemical sensors made from the as-obtained α-MoO_3 nanoplates show an enhanced and selective gas-sensing performance to ethanol vapors. The α-MoO_3 nanoplate sensors reach a high sensitivity of 44–58 for an 800 ppm-ethanol vapor operating at 260–400 °C, and their response times are less than 15 s. The topochemical process proposed here is suitable for large-scale synthesis of α-MoO_3 nanoplates because the microstructures of the final α-MoO_3 nanoplates are insensitive to the processing parameters. Besides the gas-sensing application, the as-obtained α-MoO_3 nanoplates have potential applications in catalysts.

Acknowledgements

This work was supported by the National Natural Science Foundation of China (Grant No. 50802090), the China Postdoctoral Science Foundation (Grant No. 20090450094, Grant No. 201003397), the Opening Project of State Key Laboratory of High Performance Ceramics and Superfine Microstructure (Grant No. SKL200905SIC), and the Introduced Talent Project of Zhengzhou University.

References

1 N. A. Chernova, M. Roppolo, A. C. Dillon and M. S. Whittingham, *J. Mater. Chem.*, 2009, **19**, 2526.
2 L. Zheng, Y. Xu, D. Jin and Y. Xie, *Chem. Mater.*, 2009, **21**, 5681.
3 A. Wisitsoraat, D. Phokharatkul, A. Tuantranont and C. Saikaew, *IEEE Sensors*, 2009, **1–3**, 312.
4 E. Comini, L. Yubao, Y. Brando and G. Sberveglieri, *Chem. Phys. Lett.*, 2005, **407**, 368.
5 W. S. Kim, H. C. Kim and S. H. Hong, *J. Nanopart. Res.*, 2010, **12**, 1889.
6 M. B. Rahmani, S. H. Keshmiri, J. Yu, A. Z. Sadek, L. Al-Mashat, A. Moafi, K. Latham, Y. X. Li, W. Wlodarski and K. Kalantar-zadeh, *Sens. Actuators, B*, 2010, **145**, 13.
7 Z. X. Song, N. Mimura, J. J. Bravo-Suarez, T. Akita, S. Tsubota and S. T. Oyama, *Appl. Catal., A*, 2007, **316**, 142.
8 F. Wang and W. Ueda, *Chem. Commun.*, 2008, 3196.
9 L. Cheng, M. W. Shao, X. H. Wang and H. B. Hu, *Chem.–Eur. J.*, 2009, **15**, 2310.
10 F. Wang and W. Ueda, *Chem.–Eur. J.*, 2009, **15**, 742.
11 S. H. Lee, Y. H. Kim, R. Deshpande, P. A. Parilla, E. Whitney, D. T. Gillaspie, K. M. Jones, A. H. Mahan, S. B. Zhang and A. C. Dillon, *Adv. Mater.*, 2008, **20**, 3627.
12 L. Q. Mai, B. Hu, W. Chen, Y. Y. Qi, C. S. Lao, R. S. Yang, Y. Dai and Z. L. Wang, *Adv. Mater.*, 2007, **19**, 3712.
13 C. V. S. Reddy, Z. R. Deng, Q. Y. Zhu, Y. Dai, J. Zhou, W. Chen and S. I. Mho, *Appl. Phys. A: Mater. Sci. Process.*, 2007, **89**, 995.
14 S.-M. Paek, J.-H. Kang, H. Jung, S.-J. Hwang and J.-H. Choy, *Chem. Commun.*, 2009, 7536.
15 M. F. Hassan, Z. P. Guo, Z. Chen and H. K. Liu, *J. Power Sources*, 2010, **195**, 2372.
16 V. M. Mohan, H. Bin and W. Chen, *J. Solid State Electrochem.*, 2010, **14**, 1769.
17 T. Brezesinski, J. Wang, S. H. Tolbert and B. Dunn, *Nat. Mater.*, 2010, **9**, 146.
18 J. Zhou, N. S. Xu, S. Z. Deng, J. Chen, J. C. She and Z. L. Wang, *Adv. Mater.*, 2003, **15**, 1835.
19 A. Khademi, R. Azimirad, A. A. Zavarian and A. Z. Moshfegh, *J. Phys. Chem. C*, 2009, **113**, 19298.

20 J. W. Rabalais, R. J. Colton and A. M. Guaman, *Chem. Phys. Lett.*, 1974, **29**, 131.
21 S. R. Dhage, M. S. Hassan and O. B. Yang, *Mater. Chem. Phys.*, 2009, **114**, 511.
22 L. Fang, Y. Y. Shu, A. Q. Wang and T. Zhang, *J. Cryst. Growth*, 2008, **310**, 4593.
23 G. C. Li, L. Jiang, S. P. Pang, H. R. Peng and Z. K. Zhang, *J. Phys. Chem. B*, 2006, **110**, 24472.
24 C. Diaz, V. Lavayen and C. O'Dwyer, *J. Solid State Chem.*, 2010, **183**, 1595.
25 B. Hu, L. Q. Mai, W. Chen and F. Yang, *ACS Nano*, 2009, **3**, 478.
26 X. K. Hu, Y. T. Qian, Z. T. Song, J. R. Huang, R. Cao and J. Q. Xiao, *Chem. Mater.*, 2008, **20**, 1527.
27 Y. L. Xie, F. C. Cheong, Y. W. Zhu, B. Varghese, R. Tamang, A. A. Bettiol and C. H. Sow, *J. Phys. Chem. C*, 2010, **114**, 120.
28 T. Siciliano, A. Tepore, E. Filippo, G. Micocci and M. Tepore, *Mater. Chem. Phys.*, 2009, **114**, 687.
29 A. M. Taurino, A. Forleo, L. Francioso, P. Siciliano, M. Stalder and R. Nesper, *Appl. Phys. Lett.*, 2006, **88**, 152111.
30 V. V. Atuchin, T. A. Gavrilova, V. G. Kostrovsky, L. D. Pokrovsky and I. B. Troitskaia, *Inorg. Mater.*, 2008, **44**, 622.
31 C. V. S. Reddy, E. H. Walker, S. A. Wicker, Q. L. Williams and R. R. Kalluru, *J. Solid State Electrochem.*, 2009, **13**, 1945.
32 I. Navas, R. Vinodkumar, K. J. Lethy, A. P. Detty, V. Ganesan, V. Sathe and V. P. M. Pillai, *J. Phys. D: Appl. Phys.*, 2009, **42**, 175305.
33 A. Michailovski, J. D. Grunwaldt, A. Baiker, R. Kiebach, W. Bensch and G. R. Patzke, *Angew. Chem., Int. Ed.*, 2005, **44**, 5643.
34 A. Michailovski and G. R. Patzke, *Chem.–Eur. J.*, 2006, **12**, 9122.
35 G. Wang, Y. Ji, L. H. Zhang, Y. M. Zhu, P. I. Gouma and M. Dudley, *Chem. Mater.*, 2007, **19**, 979.
36 K. Kalantar-zadeh, J. S. Tang, M. S. Wang, K. L. Wang, A. Shailos, K. Galatsis, R. Kojima, V. Strong, A. Lech, W. Wlodarski and R. B. Kaner, *Nanoscale*, 2010, **2**, 429.
37 D. Mariotti, H. Lindstrom, A. C. Bose and K. Ostrikov, *Nanotechnology*, 2008, **19**, 495302.
38 H. X. Bai, X. H. Liu and Y. C. Zhang, *Mater. Lett.*, 2009, **63**, 100.
39 A. Phuruangrat, D. J. Ham, S. Thongtem and J. S. Lee, *Electrochem. Commun.*, 2009, **11**, 1740.
40 M. H. Kim, B. Lee, S. Lee, C. Larson, J. M. Baik, C. T. Yavuz, S. Seifert, S. Vajda, R. E. Winans, M. Moskovits, G. D. Stucky and A. M. Wodtke, *Nano Lett.*, 2009, **9**, 4138.
41 C. V. Krishnan, J. L. Chen, C. Burger and B. Chu, *J. Phys. Chem. B*, 2006, **110**, 20182.
42 B. Yan, Z. Zheng, J. X. Zhang, H. Gong, Z. X. Shen, W. Huang and T. Yu, *J. Phys. Chem. C*, 2009, **113**, 20259.
43 A. Okada, M. Yoshimura and K. Ueda, *Appl. Phys. Lett.*, 2007, **90**, 203102.
44 S. Hu and X. Wang, *J. Am. Chem. Soc.*, 2008, **130**, 8126.
45 S. Hu, X. Ling, T. Lan and X. Wang, *Chem.–Eur. J.*, 2010, **16**, 1889.
46 F. Farzaneh and M. Najafi, *Pol. J. Chem.*, 2009, **83**, 1523.
47 W. Merchan-Merchan, A. V. Saveliev and M. Desai, *Nanotechnology*, 2009, **20**, 475601.
48 Y. P. Li, Y. X. Xiang, X. W. Dong, J. Q. Xu, F. Ruan and Q. Y. Pan, *J. Solid State Chem.*, 2009, **182**, 2041.
49 T. Itoh, I. Matsubara, W. Shin, N. Izu and M. Nishibori, *Mater. Chem. Phys.*, 2008, **110**, 115.
50 T. Itoh, I. Matsubara, W. Shin and N. Izu, *Mater. Lett.*, 2007, **61**, 4031.
51 M. Afsharpour, A. Mahjoub and M. M. Amini, *J. Inorg. Organomet. Polym. Mater.*, 2009, **19**, 298.
52 M. Niederberger, F. Krumeich, H. J. Muhr, M. Müller and R. Nesper, *J. Mater. Chem.*, 2001, **11**, 1941.
53 O. Y. Posudievsky, S. A. Biskulova and V. D. Pokhodenko, *J. Mater. Chem.*, 2002, **12**, 1446.
54 K. Shao, H. M. Luo and H. Q. Cao, *J. Mater. Res.*, 2008, **23**, 2602.
55 Y. Jing, Q. Y. Pan, Z. X. Cheng, X. W. Dong and Y. X. Xiang, *Mater. Sci. Eng., B*, 2007, **138**, 55.
56 S. Li, C. Shao, Y. Liu, S. Tang and R. Mu, *J. Phys. Chem. Solids*, 2006, **67**, 1869.
57 M. I. Shukoor, H. A. Therese, L. Gorgishvili, G. Glasser, U. Kolb and W. Tremel, *Chem. Mater.*, 2006, **18**, 2144.
58 D. Chen, X. Hou, H. Wen, Y. Wang, H. Wang, X. Li, R. Zhang, H. Lu, H. Xu, S. Guan, J. Sun and L. Gao, *Nanotechnology*, 2010, **21**, 035501.
59 A. Tricoli and S. E. Pratsinis, *Nat. Nanotechnol.*, 2010, **5**, 54.
60 J. Zhang, X. H. Liu, S. H. Wu, M. J. Xu, X. Z. Guo and S. R. Wang, *J. Mater. Chem.*, 2010, **20**, 6453.
61 S. Vallejos, T. Stoycheva, P. Umek, C. Navio, R. Snyders, C. Bittencourt, E. Llobet, C. Blackman, S. Moniz and X. Correig, *Chem. Commun.*, 2011, **47**, 565.
62 Q. Xiang, G. F. Meng, H. B. Zhao, Y. Zhang, H. Li, W. J. Ma and J. Q. Xu, *J. Phys. Chem. C*, 2010, **114**, 2049.
63 R. Binions, A. Afonja, S. Dungey, D. W. Lewis, I. P. Parkin and D. E. Williams, *IEEE Sens. J.*, 2011, **11**, 1145.
64 D. Chen, X. Hou, T. Li, L. Yin, B. Fan, H. Wang, X. Li, H. Xu, H. Lu, R. Zhang and J. Sun, *Sensor. Actuat. B*, 2011, **153**, 373.
65 D. Chen and Y. Sugahara, *Chem. Mater.*, 2007, **19**, 1808.
66 G. Mestl, P. Ruiz, B. Delmon and H. Knozinge, *J. Phys. Chem.*, 1994, **98**, 11269.
67 L. Seguin, M. Figlarz, R. Cavagnat and J. C. Lassègues, *Spectrochim. Acta, Part A*, 1995, **51**, 1323.
68 D. Liu, W. W. Lei, J. Hao, D. D. Liu, B. B. Liu, X. Wang, X. H. Chen, Q. L. Cui, G. T. Zou, J. Liu and S. Jiang, *J. Appl. Phys.*, 2009, **105**, 023513.
69 L. Kondrachova, B. P. Hahn, G. Vijayaraghavan, R. D. Williams and K. J. Stevenson, *Langmuir*, 2006, **22**, 10490.
70 G. Tsilomelekis and S. Boghosian, *J. Phys. Chem. C*, 2011, **115**, 2146.
71 K. Galatsis, Y. X. Li, W. Wlodarski, E. Comini, G. Sberveglieri, C. Cantalini, S. Santucci and M. Passacantando, *Sens. Actuators, B*, 2002, **83**, 276.

